Simulation Research on the Thermal Phase Transition of EDM and the Formation Mechanism of Remelted Layer in Single Pulse Spark Discharge Crater

Jiaqian Chen*, Jianyong Liu*, Xueke Luo, Huijie Zhang, Dianxin Li, Pengyuan Kou and Ruobing Li

Department of Mechanical Engineering, Beijing Institute of Petrochemical Technology, Beijing 102600, People's Republic of China

*Corresponding author
Jiaqian Chen, Department of Mechanical Engineering, Beijing Institute of Petrochemical Technology, Beijing 102600, People's Republic of China.
Jianyong Liu, Department of Mechanical Engineering, Beijing Institute of Petrochemical Technology, Beijing 102600, People's Republic of China.

ABSTRACT

The remelted layer formed by the Electrical Discharge Machine (EDM)impacts surface quality of small hole and quality of surface finishing; it significantly reduces the fatigue life of workpieces. Based on Comsol Multiphysics, this paperusessimulates the formation process of the remelted layer under single-pulse condition. When horizontal set and two-phase flow methods are used to track the phase interface, the model is built under the coupling of flow and heat transfer fields, which simulates the solid-liquid-gas transformation during discharge etching via porous medium and weak expression methods. The simulation results show that the temperature rapidly decreases from the midpoint of the discharge center axis to the surrounding area, and the radius of the plasma region is 95.3 µm. The diameter of the pit is 108.5 µm. The thickness of the remelted layer is 16 µm. The thickness of the remelted layer obtained from experiments under the same conditions is 16.4um. The comparison shows that the difference between the two is small, indicating that the simulation model can accurately predict the thickness of the remelted layer, providing a new approach for evaluating the thickness of the remelted layer in EDM.

Introduction

The studies of EDM have focused on optimizing the machining parameters to improve the efficiency of EDM. However, the research on the physical formation of plasma channels is still not mature enough. With the development of science and the increase of industrial applications, there is increasing trend of the demand for precisioncomplex shapes [1]. EDM, as an important special machining method, has been widely used in the fields of mould-making, electronics, precision instruments, and aerospace and defense industries [2]. For some complex structural materials that are difficult to machine traditionally, conventional machining often cannot achieve low-cost machining. However, EDM often produces a thick recast layer on the surface, which leads to poor surface quality. This greatly limits its wide application in high-end fields. Therefore, it is of great significance to study the formation of plasma channels in EDM by simulation, which can help us understand the machining principles of EDM and predict surface machining.

The formation mechanism of EDM discharge channels is a key research problem in the field of EDM technology [3] . Li et al. established a discharge pit model using the simulation results of heat flux and pressure of the discharge channel model as inputs [4]. Based on simulation, the formation process and final morphology of the discharge pit were obtained, and a series of peinciple for pit formation were discovered. Somashekhar et al. found a series of laws of pit formation through electro-thermal theory and single pulse discharge research, and established a single pulse thermal simulation model [5]. They verified that the experimental results were close to the simulation. All of the above papers make a detailed study for EDM simulation, but the simulation results were not combined with the analysis of the thickness of the remelted layer, which did not achieve the effect of providing effective data for improving experimental processing. Govindan et al chieved uniform material removal, reduced diameter, and increased depth of the discharge pit in the single-pulse discharge experiment assisted by a magnetic field [6]. The positive effects of applying a magnetic field during EDM include reducing the thickness of the recast layer and improving the efficiency of plasma flushing [7,8]. Carlos Mascaraque-Ramı́rez et al. found that increasing the current intensity and penetration depth would increase the diameter of the pit through experiments [9]. The rotation of the tool would also affect the material removal rate and surface finish [10]. The above papers fully demonstrate that the effective removal of the recast layer can be achieved through a series of reliable

experimental data. In the high-speed developing era, it is no longer feasible to improve the quality of the process. Therefore, it is a reliable method to improve the machining quality by using simulation data to improve the process parameters of EDM. In this regard, it is a very effective means to use Comsol multiphysics coupling simulation to simulate the formation process of discharge channels.

Perez et al. used similar methods to determine the changes in pit size caused by single discharges.It offered valuable insights into temperature fields and induced thermal loads [11]. However, their study didn't focus on structural evolution changes and did not couple physical fields to simulate the spark erosion process. So, the temperature field results they come up with deviate from the actual results Schneider et al. proposed material and heat transfer models to simulate temperature fields induced by single discharges. Klocke F. et al. employing multiphase fields, developed a simulation model presenting realistic temperature gradients for microstructural evolution [12,13]. Lee En et al. used Comsol to establish a coupling model for single-pulse spark heat flow, investigating temperature changes and pit erosion in EDM [14]. Yadav et al. delineated the range of re-melting layers, observing continuous growth in martensite thickness and re-melting layer thickness proportional to peak current, based on simulation-derived pit temperature distributions [15]. Zhi-Wei Liu et al. segmented the EDM process into two stages, exploring temperature gradients using Comsol during the heating phase and utilizing Micress for microstructural evolution in the post-discharge re-melting phase [16]. R.Hess et al. extended existing heat transfer models to obtain actual temperature gradients for single discharges in the EDM process, calculating temperature gradients to simulate the evolution of 42CrMo4 steel structures[17,18]. Despite finite element models establishing thermal loads, insufficient depth was explored in Comsol's boundary conditions and re-melting layer thickness. The research didn't deeply integrate both aspects for analysis. Due to the complexity of EDM and the instantaneous nature of microstructural evolution, literature documents only a few simulation approaches.

In view of the lack of theoretical analysis of remelted layer thickness of EDM microfabrication, the formation mechanism of remelted layer in the microfabrication discharge process for theoretical analysis, simulation, and experimental comparative analysis, due to the EDM process is through the tip of the discharge, the final formation of the pit at the very bottom of the thickness of the remelted layer, that is, for the multi-pulse EDM consistent with the laboratory machining holes need to be removed from the remelted layer coincides with the laboratory processing of the remelted layer. According to the simulation results to obtain the temperature field calculated channel and pit diameter. The pulse-controlled discharge test program is designed to establish the analytical model of remelted layer thickness, which realizes a new breakthrough in the theory of remelted layer thickness assessment method of EDM.

Theoretical Calculation of Discharge Channels
EDM is a thermal machining process, in which the discharge channel serves as the heat source. Its characteristics directly affect the heating state of the discharge point and are the most direct factor affecting the discharge erosion. Therefore, it is

necessary to conduct in-depth research on the channel [19]. During each single spark discharge process, various complex reactions occur. Such as the formation of the plasma channel, heat radiation, heat conduction, heat convection, the implosion of the plasma channel, the formation of shock waves, the erosion of molten metal, the formation of a recast layer by resolidification, and then accompanied by electrical and chemical phenomena, as well as the interaction of various reactions [20]. In this chapter, the flow field, heat transfer field, and electromagnetic field will be coupled. The electromagnetics, fluid heat transfer, and laminar flow modules will be used to determine the heat flux and temperature distribution generated in the plasma channel. The channel diameter will be calculated through the temperature field. The heat flux and pressure at the electrode surface obtained will be used as input to establish a single-pulse spark discharge pit simulation model based on multi-physics coupling and multiphase flow motion processing methods.

Underlying Assumptions of the Model
Each discharge process in EDM is the result of the combined action of multiple physical fields. The discharge channel mainly includes three components, namely the tool electrode, the interelectrode medium, and the workpiece. The size of the discharge channel simulation model is shown in Figure 1. In order to improve the convergence of the model and reduce the computational cost of the simulation, a two-dimensional plane model is established in this paper. The y-axis is the center of symmetry of the model, and it is also the center axis of the
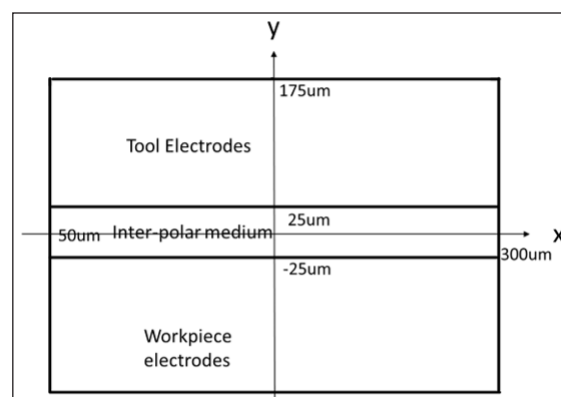

Figure 1: Dimensions of the discharge channel simulation model

The model adopts the following assumptions:
- The plasma is in local thermal equilibrium, ignoring the non-equilibrium region, and is a continuum, while the flow of the plasma is laminar and incompressible fluid.
- The electrode and the working material are homogeneous and isotropic. The properties of the working material, such as density, thermal conductivity and specific heat, are temperature dependent.
- Each discharge only produces one galvanic crater. The proportion of energy going to the cathode is a variable related to the energy of the spark.

Control Equations and Boundary Conditions of the Model
The current generated in the discharge channel generates a magnetic field, the magnetic field generated by the Lorentz force will affect the flow rate of the medium between the poles, which in turn generates different pressures and temperatures in the discharge channel, and the different temperature field in turn

affects the physical parameters of the medium, which leads to changes in the current density and the magnetic field, so that the formation of EDM channel is a multi-physical field coupling process with a more complex process. According to the above analysis, it can be seen that the model involves heat transfer field, flow field, and electromagnetic field, with reference to the following physical equations to reasonably simplify and use COMSOL software simulation to add control equations. The cited equations are as follows:

(1)   Mass conservation law model equation

$$\frac{1}{r}\cdot\frac{\partial(r\rho\mu)}{\partial r}+\frac{\partial(\rho w)}{\partial z}=0 \tag{1}$$

Formula ρ -- XDensities (kg/m³);
μ -- Radial velocity (m/s);
w -- Axial velocity (m/s).

(2)   Conservation of momentum equation Radial:

$$\frac{1}{r}\cdot\frac{\partial(r\rho uu)}{\partial r}+\frac{\partial(\rho uw)}{\partial z}=\frac{\partial p}{\partial r}+\frac{1}{r}\cdot\frac{\partial}{\partial r}(2r\eta\cdot\frac{\partial u}{\partial r})+\frac{\partial}{\partial z}(\eta(\frac{\partial w}{\partial r}+\frac{\partial u}{\partial z}))-2\eta\frac{u}{r^2}+F_r \tag{2}$$

Axial:

$$\frac{1}{r}\cdot\frac{\partial(r\rho uw)}{\partial r}+\frac{\partial(\rho ww)}{\partial z}=-\frac{\partial p}{\partial z}+\frac{1}{r}\cdot\frac{\partial}{\partial r}(r\eta\cdot(\frac{\partial w}{\partial r}+\frac{\partial u}{\partial z}))+\frac{\partial}{\partial z}(2\eta\cdot\frac{\partial w}{\partial z})+F_z \tag{3}$$

Formula η -- Coefficient of viscosity (Pa.s);
p -- Stress (Pa);
F_z -- Axial Volume Force (N/m³);
Divided into Lorentzian magnetic gravity and axial component $F_z=j_r.B_\theta-\rho g$;
F_r -- Radial Volume Force (N/m³),
Which is the radial componen of the Lorentzian magnetic force;
$F_r= -j_r.B_\theta$.

Included j_z -- Axial current density (A/m²);
j_r -- Radial current density (A/m²);
g -- Gravitational acceleration (m/s²);
B_θ -- Angle direction magnetic induction (T).

(3)   Formation of equations based on the law of conservation of energy

$$c_p(\frac{1}{r}\cdot\frac{\partial(r\rho uT)}{\partial r}+\frac{\partial(\rho wT)}{\partial z})=\frac{1}{r}\cdot\frac{\partial}{\partial r}(r\lambda\frac{\partial T}{\partial r})+\frac{\partial}{\partial z}(\lambda\frac{\partial T}{\partial z})+q_J-R \tag{4}$$

Formula c_p -- Constant-pressure specific heat (J/kg/K);
λ -- Heat conductivity (W/m/K);
q_J -- Joule heat (W/m³);
T -- Temperature (K);
R -- Radiant power per unit volume (W/m³);
σ -- Conductivity (S/m).

Based on the complexity of the model and the high temperature in the discharge channel, it is necessary to do a simple treatment under the condition of ensuring that the radiatively dissipated power is taken into account, so this model only takes into account the effect of bremsstrahlung radiation, viz:

$$R=1.54\times10^{-38}\cdot N_e\cdot\sum(N_i\cdot Z_i^2)\cdot T^{1/2} \tag{5}$$

Formula N_i -- Density of the ith ion (m⁻³);
Z_i -- Effective charge of the ith ion;
N_e -- Electron number density (m⁻³).

The electron number density is calculated based on the degree of ionization, which is calculated according to equation (6), i.e:

$$\frac{\alpha^2}{1-\alpha^2}=\frac{2.4\times10^{-4}}{p}T^{2.5}\exp(-W/KT) \tag{6}$$

Formula K -- Boltzmann constant (J/K);
W -- Atomic ionization energy (eV).

(4)   Boundary conditions for ultiphysics field simulation models
During the discharge process, the properties and structure of the workpiece material have changed. CG, DH, and GH belong to the interface between the gap medium and the external environment. To simplify the calculation, it is necessary to control the influence of the fluid boundary on the flow field in the calculation, or to neglect it. According to the heat boundary and fluid boundary conditions, it is defined as a temperature boundary and a slip boundary. AC, AB, and BD belong to the interface between the workpiece material and the external environment. Then, according to the heat source, fluid, and structural mechanics boundary conditions, they are defined as constant temperature boundary, fixed boundary, and fixed constraint. CD belongs to the heat boundary condition. Assuming that the main transmission mode of the Gaussian heat source is conduction and convection, there is heat conduction and convective heat conduction at the boundary of the discharge surface. During the entire discharge process, the workpiece material will expand in volume during the heating stage and shrink in volume after the heat source is removed. With the removal of molten material and shear flow, a discharge pit is gradually formed. According to the flow dynamics and structural mechanics boundary conditions, the discharge interface CD and EF are defined as free boundaries, and the material state changes in real time according to the change of discharge time. Table 1 summarizes the boundary conditions of the simulation model in this paper.
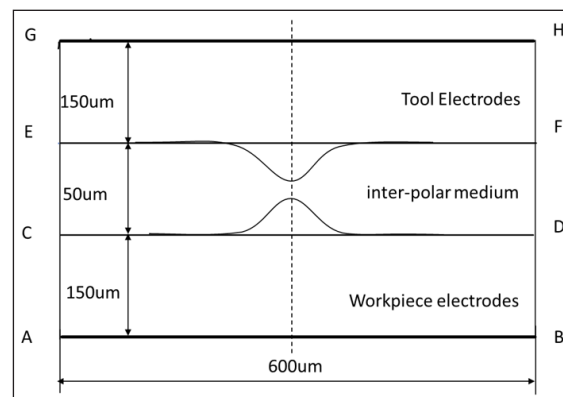

Figure 2: Schematic of the dimensions of the 2D simulation model

Table 1: Boundary conditions of the ultiphysics field simulation model

Borderline	Boundary Condition	Boundary Simulation Equations
CG, GH, DH	1. Thermal temperature boundary	$T=T_0$ (293K)
	2. Fluid: Slip-wall boundary	$u \cdot n=0$
	3. Structural mechanics:	
AC, AB, BD	1. Constant temperature boundary	$\partial T/\partial n=0$
	2. Fluid: fixed boundary	$u = 0$
	3. Structural mechanics: fixed constraints	$u_2 = 0$
CD, EF	1. Thermal convection	$k \cdot \partial T/\partial z = h_c (T\text{-}T_0)$, Formula h_c is the heat transfer coefficient T_0 at room temperature 292K$_o$
	2. Fluid: free boundary	
	3. Structural mechanics: free boundaries	

Multi-physics Field Coupling Simulation Condition Setting
The high temperature in the channel will also melt and vaporize the metal material at the discharge point, so each discharge will form a small discharge pit on the tool electrode and the workpiece electrode. The formation of the discharge pit is the combined action of the flow field and the heat transfer field. The coupling of the flow field and the heat transfer field in the simulation model can accurately simulate the real appearance of the discharge pit. During the discharge erosion process, the three-phase transformation of the solid phase, liquid phase, and gas phase will occur between the two electrodes. The phase change of the electrode material during the discharge erosion is shown in Figure 3.
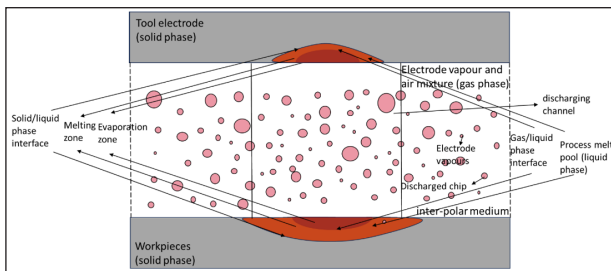

Figure 3: Schematic diagram of the phase transition of the electrode material during the discharge etching process

Basic Assumptions of Physical Processes in Simulation Models
During the electric spark discharge process, complex phase transition reactions occur in the discharge region. In order to accurately trace the morphology of the simulated discharge etch pits liquid-solid and gas-liquid phase interfaces, we use two-phase flow and level set methods. Two-phase flow is a flow problem in fluid dynamics that involves the state of matter as two phases, including solid-liquid, liquid-gas, gas-solid, and liquid-liquid (two inhomogeneously mixed liquids). Both level-set and phase-field methods are field-based methods where the phase interface is represented by an equivalent surface of the level-set or phase-field function. Since turbulence is a very random, transient flow state, the flow velocity and flow direction change from moment to moment. Therefore, the motion of the medium in the simulated discharge region is considered as a turbulent motion, and in the turbulence model, the large eddies separate into many small eddies and generate energy dissipation, which makes the detailed information of the fluid lost. Therefore, the surface tension effect becomes unimportant in the macroscopic description of the fluid. At the same time, topological changes are almost unavoidable due to the very violent flow on turbulent surfaces. Therefore, the level set method is used when combining the turbulence model with the separated multiphase flow model. Finally, the model is further processed to simplify the calculations:

1). Liquid-phase and gas-phase material flows are laminar and incompressible Newtonian viscous fluids;
2). The electrode and workpiece materials are homogeneous and isotropic and the Boussinesq assumption is used;
3). Air and electrode vapor in the gap between poles are considered to be in the same gas phase.

Simulation Model Parameter Setting
The EDM crater model mainly involves heat transfer and flow fields, and in order to better calculate and demonstrate the temperature of the model as well as the flow velocity and pressure of the fluid, the equations of conservation of mass, momentum, and energy are applied, and the coupling between the physical fields will also be involved.

In addition to utilizing the aforementioned equations for computing fundamental numerical values-such as temperature, fluid velocity, and pressure during the simulation, several pivotal considerations arise. Upon the initiation of discharge, rapid heating of the electrode material occurs. As the material attains the phase transition temperature, it undergoes a phase change, inducing alterations in the phase interface and influencing parameters within the flow field equations. Furthermore, subsequent to the material achieving the requisite temperature and undergoing phase transition, both the molten pool and electrode vapor generated during the discharge process are regarded as fluid entities. Within the molten pool, substantial temperature gradients manifest during the thermal ascent, giving rise to natural convection where material dynamics encompass not only gravitational effects but also buoyancy forces. At the interface between the gas and workpiece material, specifically, the gas-liquid phase interface, is subject to the influence of pressure in the discharge channel and surface tension. For a more precise tracking of the gas-liquid phase interface, the physical field settings within the simulation model encompass these pertinent parameters. Detailed formulations for computations will be explicated in subsequent sections. Additionally, owing to the swift occurrence of material phase transitions, this encompasses not only energy transference but also mass diffusion. To address this issue, pertinent source terms will be integrated into both the mass conservation equation and energy conservation equation, with explicit formulations elucidated in the ensuing sections.

Laminar Flow Module

The additional forces introduced in the physical layer of laminar flow simulation encompass:

Gravitational force: $\begin{cases} x=0 \\ y= \text{-g\_const(m/s}^2) \end{cases}$ (7)

Formula g_const -- Gravitational acceleration (physics),
g_const = 9.80665 m/s².

During the phase transition of the electrode material, both the solid-phase region, liquid-phase region, and the coexistence of both phases occur simultaneously. To better track the physical state of these regions during the simulation, a porous media model is employed to establish equations addressing this issue [21]. Darcy resistance is utilized to set up its equation.

Darcy damping force F_d: $\begin{cases} x=F_x*\text{phlis} \\ y=F_y*\text{phlis} \end{cases}$ (8)

Formula phils -- Level Set Variable;

$$F_x = -f \times u \times A, f = \frac{(1-alpha)^2}{(alpha^3+B)},$$

alpha -- Liquid phase volume fraction of molten material;
A -- Constant indicating the morphology of the paste zone = 1×e⁶, i.e. the larger value;
B -- a computational constant (math),
In order to avoid a zero in the denominator 1×e⁻³, i.e. the smaller value,
u -- u - axis direction vector;

$$F_y = -f \times z \times A, f = \frac{(1-alpha)^2}{(alpha^3+B)};$$

z -- z - axis direction vector.

When $^{alpha=0}$ the time, the region is a completely solid-phase area, its flow velocity is 0, that is, at this time the momentum conservation equation disappears; when $^{alpha=1}$ the time, the region is a completely liquid-phase area, the flow velocity also increases with the momentum conservation equation can also be done in the form of general equations solved; thus judging when $^{0<alpha<1}$, the region is considered to belong to solid/liquid mixing area, the paste area flow characteristics of the effect of a better. As for the liquid phase volume fraction mentioned above, due to the melting and solidification process of the phase change of the material, there will be a certain temperature range, so the model through the temperature difference to indicate its change, in order to simplify the simulation difficulty, this paper consults the relevant materials to use a linear relationship to indicate:

$$alpha = \begin{cases} 0, T<T \\ \dfrac{T-T_s}{T_l-T_s}, T_s \leq T \leq T_l \\ 1, \ T>T_l \end{cases}$$ (9)

Formula
alpha -- Liquid phase volume fraction of molten material;
T_s -- Solid phase line temperature of the material (K);
T_l -- Liquid phase line temperature of the material (K).

Due to minimal variations in the material properties of the workpiece, achieving uniformity in the physical parameters of the solid and liquid phases during phase transition is challenging. To best simulate and differentiate the changes among phases during EDM, as indicated in the above equation, when the temperature is below T_s, the liquid phase volume fraction is 0, denoting the solid phase in that region. When the temperature lies between T_s and T_p, the region represents a solid/liquid coexistence phase. Subsequently, when the temperature exceeds T_p the liquid phase volume fraction is 1, indicating a complete liquid phase region. Simultaneously, an additional transitional zone for the melting phase transition temperature will be incorporated. In this transition zone, corresponding adjustments in density, thermal conductivity, and dynamic viscosity will be applied during the phase transition. This approach enables a more precise differentiation among the changes in various phases, that is:

$\rho_v = \rho_s \times (1\text{-}alpha) + \rho_l \times alpha$ (10)
$k_v = k_s \times (1\text{-}alpha) + k_l \times alpha$ (11)
$u_v = u_s \times (1\text{-}alpha) + u_l \times alpha$ (12)

Formula ρ_v -- Solid-liquid density (kg/m³);
ρ_s -- Solid-phase density (kg/m³);
ρ_l -- Liquid-phase density (kg/m³);
k_v -- Solid-liquid-phase thermal conductivity (N.s/m²);
k_s -- Solid-phase thermal conductivity (N.s/m²);
k_l -- Liquid-phase thermal conductivity (N.s/m²);
u_v -- Solid-liquid-phase dynamic viscosity (Pa.s);
u_s -- Solid-phase dynamic viscosity (Pa.s);
u_l -- Liquid-phase dynamic viscosity (Pa.s).

The equivalent heat capacity expression for is:

$$c_p = \begin{cases} c_{ps}, T<T_s; \\ c_{ps} \times (1-alpha) + c_{pl} \times alpha + \\ \dfrac{L_f}{T_l-T_s}, T_s \leq T \leq T_l; \\ c_{pl}, T>T. \end{cases}$$ (13)

Formula L_f -- Latent heat of melting (physics) (J/kg).

The above-mentioned material properties will all be accounted for in the corresponding mathematical equations for solid/liquid phase treatment, taking into consideration the influence of phase change latent heat.

metallic buoyancy

F_f: $\begin{cases} x = 0 \\ y = \text{rho\_l} \times Bt \times (T\text{-}Tg) \times \text{g\_const} \times \text{phils} \times \text{step2} \end{cases}$ (14)

Formula rho_l -- Liquid-phase density (kg/m³);
Bt -- Coefficient of thermal expansion;
step2 -- Melting step factor
phi l s -- Level Set Variables.

Marangoni, capital of Comoros (Tw)
F_m: $\begin{cases} \text{marangoni} \times Tx \times \text{delta} \times \text{step2} \\ \text{marangoni} \times Ty \times \text{delta} \times \text{step2} \end{cases}$ (15)

Formula marangoni -- Marangoni coefficient

Metal boiling shock pressure

$$F_J: \begin{cases} F_x = \text{step3} \times \text{pressure} \times \text{delta} \times n_x \times \text{phils} \\ F_y = \text{step3} \times \text{pressure} \times \text{delta} \times n_y \times \text{phils.} \end{cases} \qquad (16)$$

Formula pressure -- Recoil pressure (pa),

$$\text{pressure} = \frac{(1 + \text{ntr})}{2} \times P\_satc;$$

$$s\_n = \sqrt{\text{philsx}^2 + \text{philsx}^2 + \text{eps}};$$

$$n_x = \frac{\text{philsx}}{s\_n};$$

$$n_y = \frac{\text{philsy}}{s\_n}.$$

In the level-set physical field setup, the level-set equations' complementary source terms are corrected by a weak expression,

$$-\text{test(phils)} \times \text{phisourcec} \times \text{step4} \times \text{usourcec} \times \text{step4} \qquad (17)$$

Formula phils -- Level Set Variables;
phisourcec -- Level Set Updates,

$$\text{phisourcec} = -\frac{m}{t} \times \text{delta} \times \left(\frac{V_1}{\rho_1} - \frac{V_2}{\rho_2}\right);$$

usourcec -- The energy conservation equation introduces a source term,

$$\text{usourcec} = \text{mdotc} \times \text{delta} \times \frac{(\rho_2 - \rho_1)}{(\rho_2 \times \rho_1)};$$

$\frac{m}{t}$ − −Rate of evaporation，delta − −Level Set Specific Function Interface,
V -- Volumetric, ρ -- Density.

$$\begin{cases} 2 \times \pi \times r \times \phi_{\text{crosswind}} \\ 2 \times \pi \times r \times \phi_{\text{streamline}} \\ 2 \times \pi \times r \times (\phi_r \times \text{test}_{(Tr)} + \phi_z \times \text{test}_{(Tz)}) \times d \\ -2 \times \pi \times r \times C_v \times (V_r \times T_r + V_z \times T_z) \times d \end{cases} \qquad (18)$$

Included $C_v = \rho \times C_p$;
Formula $\phi_{\text{crosswind}}$ -- Side-air heat flux;
$\phi_{\text{streamline}}$ -- Streamline heat flux;
ϕ_r -- Conducted heat flux, r-component;
ϕ_z -- Conducted heat flux, z - component;
$\text{test}_{(Tr)}$ -- function (math.), Lagrangian (linear unit), r-component;
$\text{test}_{(Tz)}$ -- function (math.), Lagrangian (linear unit) z-component。

C_v -- Effective volumetric heat capacity;
ρ -- Density;
C_p -- Specific heat capacity (physics);
V_r -- Speed, r-component;
V_z -- Speed z-component;
T_r -- Temperatures r-component;
T_z -- Temperatures z-component

Considering that the source terms introduced above will be related to the evaporation rate of the material undergoing a phase change, the evaporation rate is mainly affected by the temperature and saturation vapor pressure, and based on heat loss considerations, a modified equation for energy conservation will be introduced.

$$Q_{\text{vap}} = -\text{mdotc}*\text{Lstre}*\text{delta} \qquad (19)$$

mdotc is rate of evaporation,

$$\text{mdotc} = \sqrt{\text{amu} \times \frac{\text{proton}}{2\pi \times Kb \times T}} \times P\_satc \times (1\text{-ntr})$$

According to the Clausius-Clapeyron law,
P_satc is the saturated vapour pressure,

$$P\_satc = P_0 \times \sqrt{\frac{amu \times proton \times L_v \times (T - T_v)}{K_b \times T \times T_v}}$$

delta is a level-set-specific function interface,

$$\text{delta} = 6 \times \text{tpf} \cdot \text{vf2} \times (1\text{-tpf} \cdot \text{vf2}) \frac{1}{2} \cdot \sqrt{\text{philsr}^2 + \text{phisz}^2 + \text{eps}}$$

Formula
amu -- Relative atomic mass;
proton -- Monatomic mass;
Kb -- Boltzmann's constant;
ntr -- Counter-diffusion coefficient
L_v -- Latent heat of evaporation (physics);
L_f -- Latent heat of melting (physics);
C_s -- Solid-phase specific heat capacity (J/(kg.K));
C_f -- Liquid-phase specific heat capacity (J/(kg.K);
Lstre -- Latent heat introduced by evaporation rate,
Lstre = $L_v + L_f + C_s \times (T_g - T_{li}) + C_f \times (T_v - T_l)$;
Included T_g -- Solid-phase line temperature (K);
T_{li} -- Ambient temperature (K), 293.15K;
T_v -- Boiling-line temperature (K) T_l -- Liquid-phase line temperature (K)

According to the above source term analysis, in order to study the tool and medium surface and medium and workpiece surface material changes, the phase interface changes have been able to get a more accurate tracking, but at the same time, we should also take into account the molten pool surface subjected to the role of tension, the simulation formula is as follows:

$$F = \begin{cases} x = \text{tensiont} \times \text{delta} \times \text{tar} \times \text{na}; \\ y = \text{tensiont} \times \text{delta} \times \text{tar} \times \text{nb}; \end{cases} \qquad (20)$$

tensiontis is the surface tension coefficient is introduced into the equation;
delta -- interface incremental function;
tar -- horizontal set interface curvature;
na -- interface normal (x-component);
nb -- interface normal (y-component).

Horizontal Set Method Setting
The level set method expresses evolving curves or surfaces in lower dimensions through higher-dimensional function surfaces. It indirectly represents the evolving interface by using the zero-level set of a higher-dimensional level set function. Transforming

the evolution equation of the evolving curves or surfaces into an evolution partial differential equation of the higher-dimensional level set function enables capturing the moving boundaries by solving equations concerning the level set function. In essence, elevating the computational dimension enhances precision. This method can be easily extended to arbitrary dimensional spaces. One current application involves integrating the level set method with active contour models, using it to solve the partial differential equations obtained from the active contour model.

During the simulation process, the function values at various points continuously change. The value of the level set function at any arbitrary point within the molten pool flow is determined by the distance from that point to the phase interface. The tracking method is represented in the equation below:

$$\frac{\partial I_s}{\partial t} + u \cdot \nabla I_s = V_{is} \nabla \cdot (h_{is} \nabla I_s - I_s (1 - I_s) \frac{\nabla I_s}{|\nabla I_s|}) \quad (21)$$

Formula I_s -- Level set function
V_{is} -- Re-initialisation speed (m/s);
h_{is} -- Phase transition speed (m).

Considering significant differences in material properties across both sides of the phase interface, complex computational requirements pose substantial engineering challenges. To streamline the equations, the introduction of the Heaviside function is proposed for defining specific material properties, facilitating a smoother transition. Additionally, a weak formulation will be incorporated for precise handling of interface capture and smooth computations. The expressions are as follows:

$$\begin{cases} \varepsilon \times philst \times test(phils) \\ test(philsx) \times cap_x + test(philsy) \times cap_y \\ test(phils) \times (V_x + V_y) \\ S_{is} \\ C_{is} \end{cases} \quad (22)$$

Formula
ε -- Porosity;
philst -- Horizontal set vector and;
test(*phils*) -- Horizontal Set Variable Trial Function;
test(*philsx*) -- Level set variable trial function, x-component;
cap_x -- Auxiliary variable x-component;
V_x -- Speed x-component;
S_{is} -- Streamlined Horizontal Set;
C_{is} -- Streamlined Horizontal Set.

Discharge Crater Simulation Results and Analysis
Based on the simulation of discharge craters and considering factors like heat sources, pressure inputs, and boundary conditions, we utilized the thermal field simulation results as input for the flow field simulation. This approach allows for a more accurate crater shape and a more realistic simulation of the discharge crater formation process. By employing the most precise energy distribution ratio calculation, we can determine the energy distribution of the heat source. Furthermore, we can ascertain the depth and radius of the discharge crater based on the temperature distribution.

Modelled heat sources and specific processing data
To improve the simulation of laboratory EDM conditions, we incorporated the heat source, machining material parameters, and pressure inputs into the simulation model. Subsequently, the results were computed utilizing the heat flux at the electrode surface, employing identical discharge parameters. Table 2 displays the input values utilized for the model simulation.

Table 2: Discharge crater simulation values

parameters	numerical value
electric discharge current /A	12
discharge voltage /V	110
pulse width /us	60
Height of tool electrode /um	150
Height of workpiece electrode /um	50
Height of inter-polar medium /um	150
Tools - workpiece materials	Copper-Steel
inter-polar medium	air
simulation time /us	120

Based on the simulation conditions outlined in the table, during the EDM process, the discharge energy predominantly concentrates and dissipates around the tool electrode, the processed workpiece, and the dielectric medium. This energy distribution plays a pivotal role in investigating the EDM mechanism. Specifically, the energy allocated to the tool electrode and the workpiece surface directly influences material removal and the resulting surface quality. These factors significantly impact the material removal rate and the quality of the machined surface, thereby shaping the morphology of the galvanic pits. To achieve a heat source simulation that closely resembles EDM conditions, three distinct heat source equations are introduced to overlay their effects, as represented in Equation:

$$Q_1 = Q_{cap}.B \quad (23)$$
$$Q_2 = Q_{T_2}. delta.T(t).B \quad (24)$$
$$Q_3 = h_0 \cdot (T_0 - T).delta.T'(t).B \quad (25)$$

Formula
Q_{cap} -- Modified equation for conservation of energy (W/m³),
Q_{vap} =- mdotc*Lstre*delta;
Included mdotc -- Evaporation rate,

$$mdotc = \sqrt{amu \times \frac{proton}{2\pi \times Kb \times T}} \times P\_satc \times (1-ntr);$$

delta -- A level-set specific function interface,

$$delta = 6 \times tpf \cdot vf2 \times (1-tpf \cdot vf2)\frac{1}{2} \cdot \sqrt{philsr^2 + phisz^2 + eps};$$

Lstre -- Latent heat introduced by evaporation rate,
Lstre=L_v+L_f+$C_s \times (T_g - T_{li})$+$C_f \times (T_v - T_l)$;
T_g -- Solid-phase line temperature (K)
T_{li} -- Ambient temperature (K), 293.15K;
T_v --"Boiling-line temperature (K);
T_l -- Liquid-phase line temperature (K);
B -- Volume factors from spatial to material coordinate systems;
$$Q_{T_2} = \frac{4.57 \cdot F_c \cdot U \cdot I}{\pi \cdot R_t^2}, F_c - -\text{Cathode Energy Fraction},$$

U -- Input voltage, I -- Electric current.

$$R_t = \begin{cases} d_1 + (d_2 - d_1) \cdot \dfrac{t}{3} & 0 < t < 3\mu s \\ d_2 & 3 < t < 50\mu s \end{cases} \qquad (26)$$

Formula

T(t), T'(t) -- Step function (math.);

h_0 -- Air convection heat transfer coefficient;

T_0 -- Initial temperature value.

Model simulation results and analysis

According to the heat source parameters set above to simulate the formation process of the discharge crater, the simulation time is 120us, of which the pulse width is 60us (equivalent to the application time of the heat source), as shown in Figure 4. For the formation process of the crater on the local electrode of the tool and the local electrode of the workpiece.
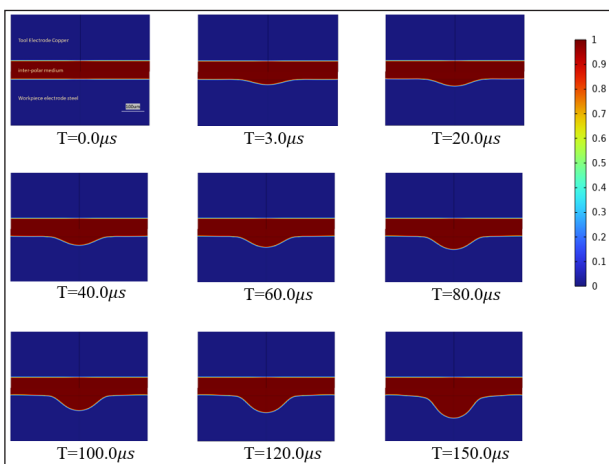
Figure 4: Diagram of electrode discharge crater formation process

Temperature field distribution of simulation results

During the EDM process, the temperature of the workpiece surface rises instantaneously within the pulse width, and the temperature field of the workpiece cannot reach a steady state due to the short time. Therefore, the temperature field formed on the workpiece surface is a transient temperature field, and the Gaussian heat density cross-section is shown in Figure 5(a), where the initial energy distribution of the discharge crater is shown in Figure 5(b).
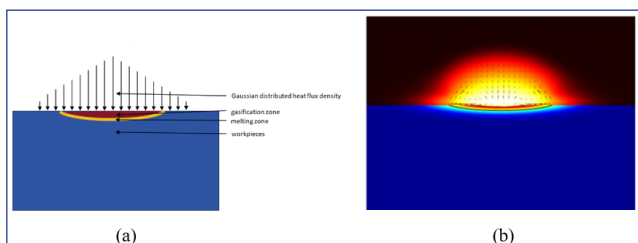

Figure 5: Schematic of Gaussian heat density in the initial phase of the discharge crater; (a) theoretical Gaussian heat density cross section; (b) simulated Gaussian heat density cross section.

Figure 6 illustrates the temperature field distribution simulation results, the maximum temperature within the discharge channel reaches 32590.9 K. Moving from the midpoint between the poles towards the surrounding areas, there's a rapid decrease in temperature. Specifically, at the radial line along the discharge channel's central axis, located between the midpoint of the poles, the temperature drops to 5000 K within a radius of 95.3 um. Typically, regions above 5000 K are considered plasma zones, thus defining the plasma region within a radius of 95.3 um in this EDM simulation [22]. Consequently, the plasma region in this EDM simulation spans a radius of 95.3 um.
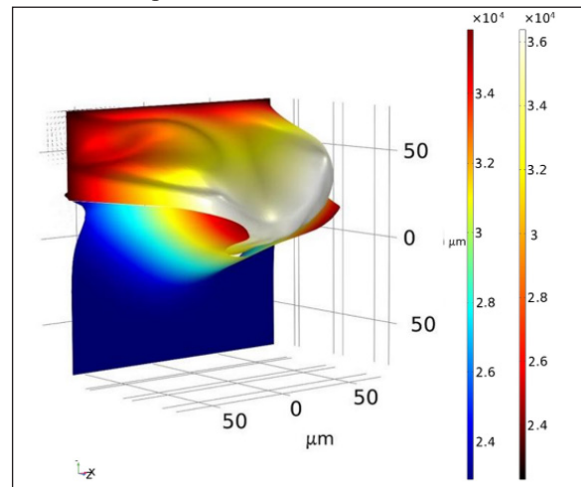

Figure 6: Temperature field distribution of simulation results

When the positive energy distribution coefficient F_a = 0.23, the diameter of the galvanic pits calculated under different processing conditions is closest to the actual measured value [23]. Where R (t) is the channel radius, not only related to the model setup size, in the processing process will be increased with time and the channel expansion phenomenon, that is, the channel radius will be enlarged, in the channel after the completion of the expansion of the radius will no longer change, set the expansion time of 3us, that is, the discharge channel in the first 3us is a linear expansion, and then to maintain the value is unchanged.

$$R_t = \begin{cases} d_1 + (d_2 - d_1) \cdot \dfrac{t}{3} & 0 < t < 3\mu s \\ d_2 & 3 < t < 50\mu s \end{cases} \qquad (27)$$

Velocity field distribution of simulation results

Figure 7 illustrates the temporal evolution of the velocity field distribution within the interpole medium region. The simulation treats the discharge channel as a fluid without accurately modeling the phase transition of individual materials or ion motion within the channel. The medium's flow in the simulation is attributed to the imbalance between the radial pressure gradient and Lorentz magnetic force. The changes in size and extent of the velocity field during the simulation are depicted in the figure. During the initial 3us, rapid expansion of the discharge channel occurs with high and unstable velocities at its sides. After 3us, the channel stabilizes its expansion, and its radius remains constant. The heat source concentrates mainly within the 95.3um radius channel. Between 3us to 60us, a more stable velocity vortex emerges, correlating with increased crater depth and diameter. After 60us, as the heat source ceases, the plasma channel vanishes, marking the end of micro-fine EDM processing. Despite the disappearance of the discharge channel, residual heat on the crater's surface, impacted by various forces like surface tension, erodes compounds from their original position, forming the crater. Different forces act on these compounds. Some may be

extruded due to strong pressure and precipitate at the bottom of the dielectric tank, while others settle on the workpiece's surface, forming spherical bumps. Consequently, the recast layer primarily comprises compounds from the original workpiece surface, wear material from the tool electrode, and a mixture of cracked liquid dielectric, recondensed afterward. The arrow in the figure denotes the dielectric flow direction between the poles, with the arrow's size indicating velocity magnitude, peaking at approximately 4 m/s.
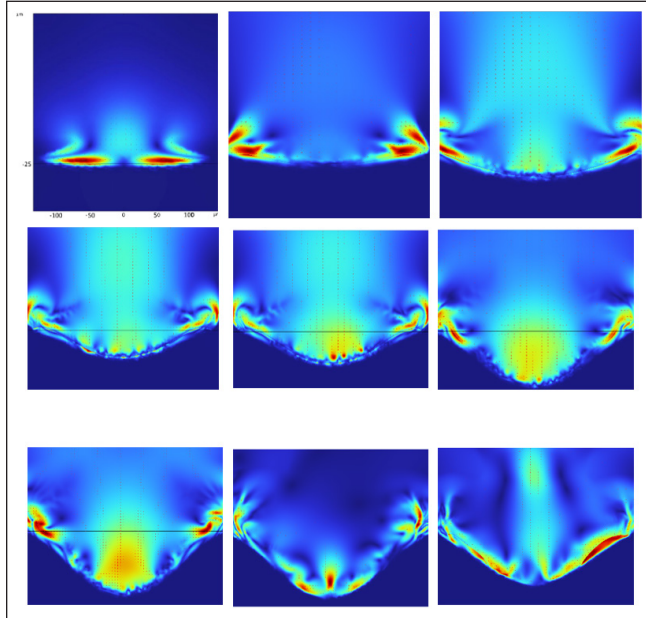
Figure 7: Velocity field distribution results for each time period in the simulated inter-polar medium region

In this research, based on simulation values from laboratory processing, Figure 4.displays the discharge crater results, indicating the crater's depth and diameter over time. Due to copper's high thermal conductivity compared to steel, the heat rapidly transfers to the copper substrate. As a result, the copper tool electrode exhibits minimal crater formation throughout the process, leading to a relatively low copper electrode loss rate. Hence, tracking the trend of the steel workpiece electrode's crater during the discharge process is vital to understanding the crater's diameter and depth, as depicted in Figure 8.The EDM surface undergoes various stages: plasma discharge channel formation, channel expansion, heat source thermal action, workpiece surface morphology alteration, and plasma discharge channel disappearance. Initially, within the first 3 us, the crater's depth and diameter rapidly increase due to the discharge channel's swift expansion and concentrated energy generation (Figure 7.). Following this, from 3 us to 10 us, although the diameter increase slows, both diameter and depth continue to rise steadily. This trend persists until 60 us, marking the heat source's conclusion. Afterward, there's a slight ongoing increase in pit diameter and depth due to residual heat impact until approximately 65 us when their dimensions stabilize. Around 45 us, noticeable changes occur not only in the pit's diameter and depth but also on the workpiece electrode's surface, where distinct raised edges appear on both sides of the pit. By 70 us, the pit surface loses its smoothness, recondensing a remelted layer attached to the pit's surface, leading to a minor reduction in pit depth.
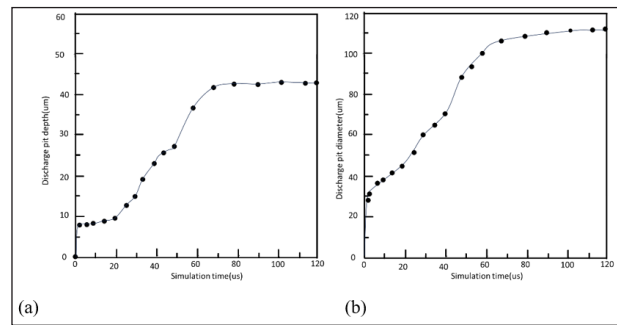

Figure 8: Variation curve of crater with simulation time;(a) variation curve of pit depth with simulation time;(b) variation curve of pit diameter with simulation time 4 Combined with the simulation results of remelted layer thickness analysis and experimental verification

Theoretical Analysis of Remelted Layers
The formation of the remelt layer encompasses gasification, melting, and solidification, involving a blend of workpiece material, electrode remnants, and cracked working fluid, thus differing notably from the substrate part of the workpiece. Furthermore, the workpiece material type dictates the organization of the remelt layer. Figure 9. and Figure 10. respectively depict the surface area distributions for micro-fine EDM and theoretical pit machining. Studies indicate that after intense heating and rapid cooling, a fraction of melted and evaporated material is removed, leaving the bulk of the melted material to constitute the remelted layer [24]. During the cooling phase of discharge, near the discharge point, the temperature steeply declines, leading the remaining molten material on the crater surface to gradually re-solidify. This results in the formation of a layer adhering to the machined holes' surface, namely the remelted layer, once cooled to room temperature. The presence of carbon material at the workpiece electrode generates a remelted layer in EDM machining primarily composed of residual austenite and martensitic columnar structures, exhibiting twice the hardness of ferrite steel (the parent material). This topmost layer, exposed to the environment, significantly impacts the machined sample properties. Microscopic examination reveals that the remelted layer possesses distinct metallographic and microstructural characteristics from the workpiece material. Studies by Rebelo et al. and Kruth et al. experimentally confirm the remelted layer's fine-grained nature, high hardness, and brittleness, emphasizing its substantial influence on machined surface roughness improvement through its removal [25,26].

Internal bumps, and pits within the remelt layer contribute to increased surface roughness, along with microcracks. Hasçalık correlates surface crack density with the remelt layer's average thickness, indicating lower surface crack density with thicker remelt layers [27]. Alternating loads on parts might propagate into the blade matrix, potentially causing fractures. Oxidation-induced spalling of the recast layer at high temperatures hastens component wear, reducing part longevity. While existing studies mainly employ experimental techniques like optical metallography, SEM, and x-ray diffraction, the rapid and intricate nature of the EDM process makes direct microscopic observation and evolution through experiments nearly unfeasible. Simulation stands as a potent tool for visualizing these microphysical processes, providing a theoretical framework for related experimental research.
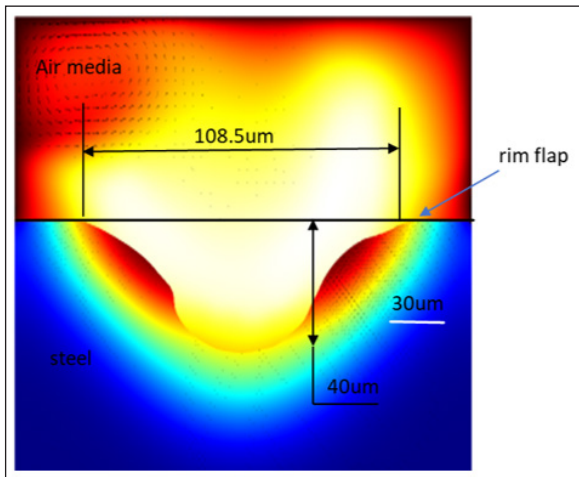
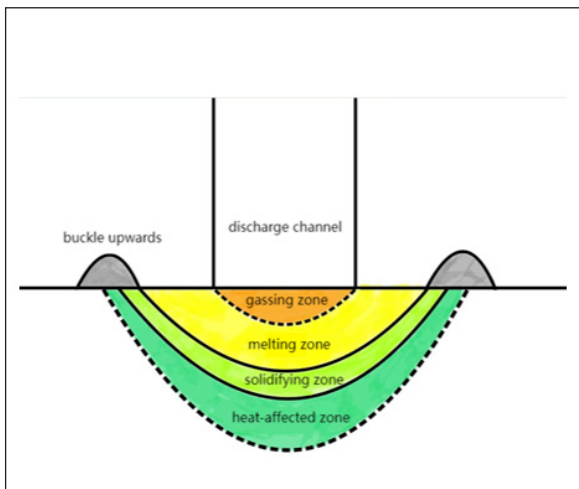**Figure 9:** Map of the simulated crater surface area

Figure 10: Theoretical pit machining workpiece surface area map

The microstructure of the remelted layer and the heat affected zone depends on the temperature distribution around the discharge pit, i.e., as the temperature applied by the heat source changes, there is a complex metallurgical phase transformation during EDM, and the microstructure of the discharge pit surface changes, and the metallurgical phase transformation process is split into two stages: the first stage is the heating stage, and when the temperature is higher than 995 K the microstructure undergoes a significant change, i.e., the two types of organizations constituting the parent material Between the percentage content will change, and when the temperature is higher than 1253 K, the phase becomes α + β → β; the second stage for the cooling phase, that is, after the disappearance of the heat source, when the temperature is lower than 1073, the phase becomes β → α ', that is, transformed into martensite process [28]. At a temperature gradient of > 80 K/s, a fully martensitic organization is obtained [29]. Therefore the remelted layer produced during EDM is mainly composed of residual austenite and martensitic columnar structure [30]. The process of microstructural change is shown in Figure11.
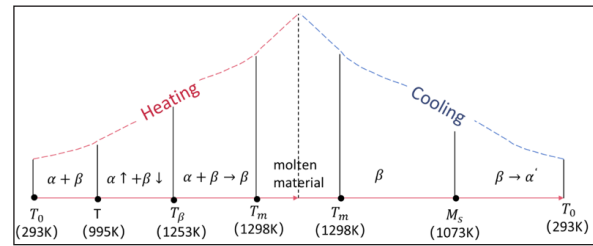

Figure 11: Microstructure change process diagram [28]

Figure 12. (a) and (b) shows the 30th and 90th us of simulated EDM, for the heating stage, which is the stage where the melting zone expands sharply and the metallurgical phase transformation is mainly reflected in the heat-affected zone, and only a small portion of the material undergoes a complete transformation from α + β → β on the surface of the crater, and the majority of the material is still in the form of α + β in the form of the two phases, but the volume fractions of these phases will be altered. Fig 12 (c) and (d) illustrate the simulated EDM at 120us and 150us, respectively. During the cooling stage, no discernible difference is evident in the temperature distribution graph. However, the tissue distribution within it becomes increasingly intricate. As the temperature drops below 1298K, the molten material adjacent to the melting zone boundary solidifies again, effectively reconstructing the martensite structure. Upon reaching room temperature, the surface tissue distribution of the discharge pit becomes evident, displaying a distinct boundary indicative of the remelted layer formation. This delineation signifies an enhancement in surface hardness attributed to the creation of a high-hardness martensitic remelted layer.
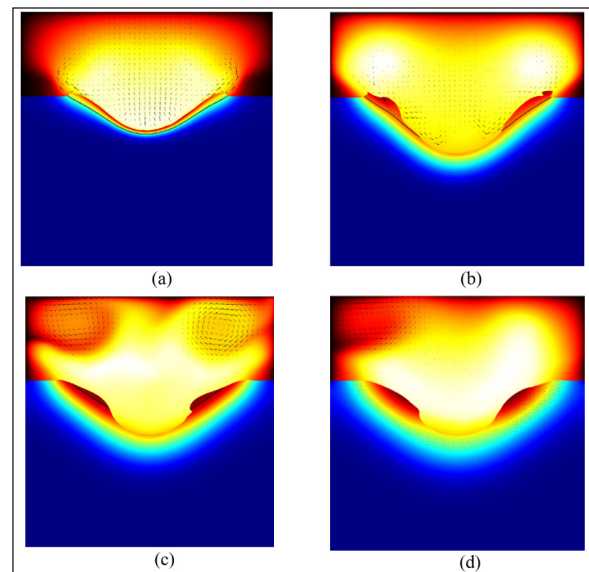

Figure 12: Simulated EDM temperature graph;(a) simulation of 30th us; (b) simulation of 90th us; (c) simulation of 120th us; (d) simulation of 150th us

Validation and Optimisation with Experimental Data
To validate the discharge crater model's simulation outcomes, EDM experiments were conducted using a pulse discharge experimental apparatus. These experiments aimed to analyze the discharge crater's morphology and measure its resulting dimensions. Considering EDM occurs via tip discharge, it's noted that the hydrostatic pressure of the melt zone decreases as it moves farther from the crater's centerline. Additionally,

the splash velocity of ejected debris in the crater's periphery is considerably lower than that at the crater center [25]. This observation implies that the remelted layer thickness at the crater center mirrors the surface characteristics of a single pulse EDM crater. As such, it doesn't impact the comparison between this experiment and the simulation results for verification. The experimental processing parameters are detailed in Table 3:

Table 3: Experimental conditions

Parameters	Numerical value
Electric discharge current /A	12
Electric discharge gap /um	50
Electrode - workpiece materials	Copper-Steel
Inter-polar medium	air
Voltage amplitude /V	110
Pulse width /us	20-80

In ensuring the experimental results' credibility, given the inherent randomness in EDM discharge delay times, test parameters were meticulously selected. This approach aimed to maintain consistency with simulation parameters while solely altering the pulse width to achieve varying discharge durations for the discharge pit. This deliberate variation ensured the model's reliability. The laboratory's EDM processing machine utilized in the experiments is depicted in Figure 13., while Figure 14. provides detailed imagery of the electrode wire used in the experiments based on the aforementioned experimental data for EDM processing.

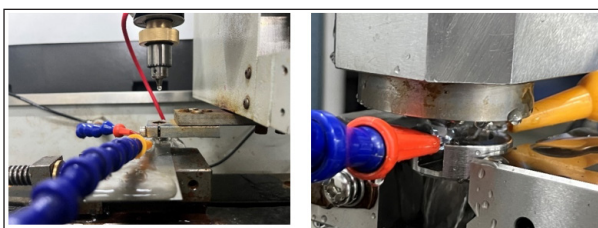**Figure 13:** Experimental EDM machine for small hole machining

Figure 14: Detailed view of small hole machining on the machine

The developed machining system, designed to address remelted layer removal, comprises several components: a worktable, guiding device, flushing liquid pipeline, transmission device, EDM spindle, drilling spindle, and a deionized water circulation system. The experimental data presented here utilizes laboratory micro-small hole composite machining equipment. The simplified overall design block diagram of the laboratory EDM-drilling composite machining system is illustrated in Figure 15.This setup employs a rotary axis post-EDM processing to retain a hole wall with a remelted layer. Subsequent hole reaming with drilling tools effectively removes the metamorphic layer from the hole wall. This process aims to achieve micro-small hole machining without a remelted layer. For enhanced efficiency in remelted layer removal, an integrated EDM spindle and drilling spindle are incorporated into the same machine for composite machining purposes. This experimental setup aims to realize remelted layer-free micro-small hole machining, utilizing drilling to ream holes post-EDM, with the primary cutting edge eliminating the remelted layer adhering to the hole wall [31].
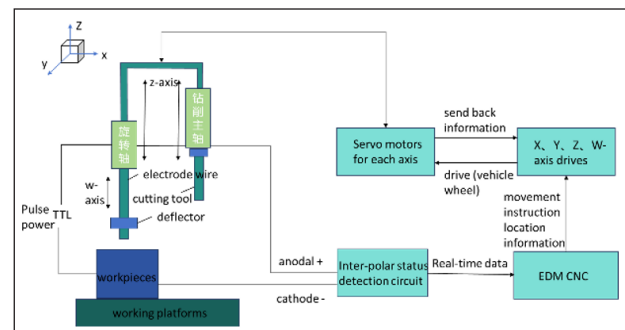

Figure 15: Block diagram of the overall design of the EDM-drilling composite machining system [31].

Given the simulation model's intricacy and the need for a more detailed observation of pit surface characteristics in EDM blind holes, the remelted layer measurements necessitated cutting open the workpiece for comparison. However, this action impacts the organizational properties on the workpiece side due to heat generation during the cutting process. This, in turn, affects the remelted layer on the machining surface. Hence, the experimental approach opted for EDM blind holes directly on the workpiece's edge. This choice aimed to minimize heat generated by other processes and its impact on both the remelted layer's thickness and the organizational properties. As the movement of the discharge channel during EDM varies each time, the distribution of the remelted layer after the solidification of the discharge channel is non-uniform, resulting in asymmetry at the edge. By utilizing simulation data from multiple processing tests, the workpiece side underwent polishing and subsequent corrosion using 4% nitric acid alcohol. This process generated several sets of small hole side profiles. The microscope was employed to observe the surface map of the side holes, as illustrated in Figure16., showcasing a comparison between the instrument-observed side hole surface and the simulated pit surface. The results of this study were provided by China Guohe General Test and Evaluation Certification JSC, No. 0220230506265.The experimentally processed EDM straight holes were formally tested, with the Institute's test results summarized in Table 4. The detection schematic is shown in Figure 17.
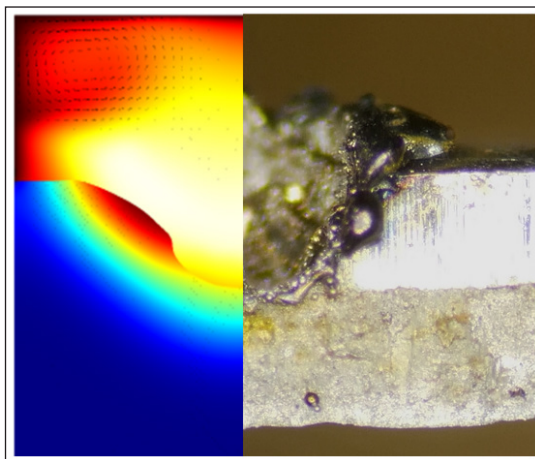
Figure 16: Comparison between experimental side hole surface and simulated pit surface. (The left half is a side profile of the simulated pit, The right half shows a side section of the experimental pit).

Table 4: Experimental product testing information

test unit	Test items	Test Methods	Test Sample Number	Test results
Guohe Tongji (Chinese company)	Remelted layer thickness	GB/T 6462-2005	GH-001 (Straight Hole EDM)	The thickness of the remelted layer is 16.4um

Figure 17: Schematic diagram of experimentally tested remelted layer thicknesses. (The three diagrams from left to right show the thickness of the remelted layer on different surfaces).

Experimental data validation

According to Comsol simulation calculations, the remelted layer thickness result is about 16um, which is basically in line with a second-order regression fitting formula between the peak current, pulse width and remelted layer thickness function i.e. [32],

$$H=1.85+0.1034A+0.1102B+0.0104AB$$

Formula A -- Peak current;
       B -- Pulse width;
       H -- Remelted layer thickness.

The thickness of the remelted layer was calculated as 17.1908 um based on the simulation data substituted into Eq.

The remelted layer thickness measured by the laboratory equipment test side holes without treatment is about 16.4um, A schematic diagram of the experimentally tested remelted layer thickness is shown in Fig. 17. Which is closer to the simulation remelted layer thickness, indicating that the model fitting effect is better, and the simulation results can be used to predict the remelted layer thickness of the experimental electrical machining small holes after machining.

Conclusion

This paper has developed a single-pulse spark discharge pit simulation model by conducting theoretical analyses. The model effectively captures the pit's temperature field, pressure field, heat flux alterations, and remelted layer formation during the machining process. Through this, the study investigates the correlation between temperature, velocity, pressure variations, and the corresponding changes in pit depth and diameter during simulation. The following conclusions have been drawn from the simulation analysis:

1. The discharge channel exhibits a maximum temperature of 32,590.9 K, rapidly declining from the interpol midpoint of the discharge center axis towards the surrounding temperature. Along the radial line situated at the interpol midpoint of the channel's center axis, the temperature drops to 5,000 K at a radius of 95.3 μm, denoting the plasma area's extent. Although the crater's dimensions persist after the plasma channel vanishes, residual heat influences the surface, resulting in recondensation. This residual heat causes recondensation on the pit surface, leading to the formation of a remelted layer.
2. The simulation indicates a remelted layer thickness of 16 μm, closely aligning with the measured thickness of 16.4 μm. The relationship between the remelted layer thickness and the experimental values of peak current and pulse width demonstrates a near match to the theoretical second-order regression fitting. This alignment suggests a strong fit of the model with the experimental outcomes.
3. Through Comsol simulation of EDM, manipulating machining parameters allows for the derivation of the pit isotherm, enabling the deduction of remelt layer thickness. This process streamlines the machining procedure, aiming to enhance machining efficiency and surface quality.
4. Partial financial support was received from Beijing Nova Program.The research leading to these results received funding from the Zhiyuan Science Foundation of BIPT under Grant Agreement No.2023003.This study was funded by he first author as well as the other named authors who have finished writing.This work was supported by the Zhiyuan Science Foundation of BIPT (Grant numbers [20230484429] and [No.2023003].

Declarations
Ethical Approval
This study did not involve human or animal subjects, and thus, no ethical approval was required. The study protocol adhered to the guidelines established by the journal.

Availability of Data and Materials
(The datasets used or analyzed during the current study are available from the corresponding author on reasonable request.)

References

1. Zhang Yongbin, Jing Qi, Wang Han. Application of micro-fine EDM technology in the manufacture of high-frequency electrical precision devices. Electro machining and Mold. 2022. 3: 1-8.

2. Chang Weijie, Chen Yuanlong. Research on diameter expansion law of single-pulse discharge channel for EDM. Journal of Mechanical Engineering. 2016. 52.

3. Guo Jianmei, He Hu, Jiang Hao, Wang Jin, Jia Zhixin. Electromagnetic field coupling model for the establishment process of discharge channel in EDM. Electrical Processing and Mould. 2022. 6: 8-11.

4. Li Xiaohui, Wei Dongbo, Yang Xiaodong. Thermofluidic simulation and experimental study of discharge channels in EDM machining. 2019. 3: 27-31.

5. Somashekhar KP, Mathew J, Ramachandran N. Electrothermal theory approach for numerical approximation of the u-EDM process. International Journal of Advanced Manufacturing Technology. 2012. 61: 1241-1246.

6. Govindan P, Gupta A, Joshi SS, Malshe A, Rajurkar KP. Single-spark analysis of removal phenomenon in magnetic field assisted dry EDM. Journal of Materials Processing Technology. 2013. 213: 1048-1058.

7. Shabgard MR, Gholipoor A, Mohammadpourfard M. Investigating the effects of external magnetic field on machining characteristics of electrical discharge machining process, numerically and experimentally. Int J Adv Manuf Technol. 2019. 102: 55-65.

8. Wang P, Li B, Shi G, Lin T, Wang B. Non-linear mechanism in electrical discharge machining process. The International Journal of Advanced Manufacturing Technology. 2018. 97: 1687-96.

9. Mascaraque-Ramirez C, Franco P. Comparison between different methods for experimental analysis of surface integrity in die-sinking electro-discharge machining processes. J. Eng. Manufacture. 2020. 234: 479-488.

10. Srinivasan VP, Palani PK. Surface integrity, fatigue performance and dry sliding wear behaviour of Si3N4-TiN after wire-electro discharge machining. Ceramics International. 2020. 46: 10734-9.

11. Pérez R, Carron J. Measurement and Metallurgical Modeling of the Thermal Impact of EDM. International Symposium on Electro machining. 2007.

12. Klocke F, Schneider S, Mohammadnejad M, Hensgen L, Klink A. Inverse Simulation of Heat Source in Electrical Discharge Machining. Procedia CIRP. 2017. 58: 1-6.

13. Klocke F, Mohammadnejad M, Hess R, Harst S, Klink A. Phase field modeling of the microstructure evolution in a steel workpiece under high temperature gradients. Procedia CIRP. 2018. 71: 99-104.

14. Li E. Simulation and experimental study of thermal-fluid coupling of EDM single-pulse discharge process. Harbin: Harbin Institute of Technology. 2021.

15. Yadav K, Pradhan SK. Analysis of recast layer thickness and martensitic layer thickness in wire electrical discharge machining. Materials Today: Proceedings. 2021. 46: 10799-10805.

16. Liu ZW, Hsu CW, Wu SH, Zhou JS, Kao JY. Performance and increased fatigue life for a Ti workpiece produced by the EDM process. The International Journal of Advanced Manufacturing Technology. 2022. 122: 1629-1639.

17. Hess R, Heidemanns L, Herrig T, Klink A, Bergs T. Model Based Prediction of the Heat Affected Zone in a Steel Workpiece Induced by an EDM Single Discharge. Procedia CIRP. 2023. 117: 263-268.

18. Schneider S, Herrig T, Klink A, Bergs T. Modeling of the temperature field induced during electrical discharge machining. CIRP Journal of Manufacturing Science and Technology. 2022. 38: 650-659.

19. Yue Xiaoming. Research on etching mechanism and surface metamorphic layer formation of EDM materials. Harbin Institute of Technology. 2019.

20. Jithin S, Raut A, Bhandarkar UV, Joshi SS. FE modeling for single spark in EDM considering plasma flushing efficiency. Procedia Manufacturing. 2018. 26: 617-628.

21. Kitamura T, Kunieda M. Clarification of EDM gap phenomena using transparent electrodes. Cirp Ann-Manuf Techn. 2014. 63: 213-215.

22. Kojima A, Natsu W, Kunieda M. Spectroscopic measurement of arc plasma diameter in EDM. CIRP annals. 2008. 57: 203-207.

23. Gao Ruiheng, Zhang Fawang, Gu Lin. Study on the energy distribution coefficient of electric spark discharge in water. Electrical Processing and Mould. 2014. 2: 1-9.

24. Yang Xiaodong, Tian Jing. High-speed camera observation of molten pool and material erosion during single pulse discharge. Electrical Processing and Mould. 2020: 7-11.

25. Rebelo JC, Dias AM, Kremer D, Lebrun JL. Influence of EDM pulse energy on the surface integrity of martensitic steels. Journal of Materials Processing Technology. 1998. 84: 90-96.

26. Kruth JP, Stevens L, Froyen L, Lauwers B. Study of the white layer of a surface machined by die-sinking electro-discharge machining. CIRP annals. 1995. 44: 169-172.

27. Jabbaripour B, Sadeghi MH, Faridvand S, Shabgard MR. Investigating the effects of EDM parameters on surface integrity, MRR and TWR in machining of Ti-6Al-4V. Machining Science and Technology. 2012. 16: 419-444.

28. Tang J, Yang X. Simulation investigation of thermal phase transformation and residual stress in single pulse EDM of Ti-6Al-4V. Journal of Physics D: Applied Physics. 2018. 51.

29. Bergs T, Mohammadnejad M, Hess R, Heidemanns L, Klink A. Simulation of the Evolutions in Real Microstructure of Material under Thermal Cycle with High Thermal Gradients. Procedia CIRP. 2020. 95: 238-243.

30. Klocke F, Mohammadnejad M, Hess R, Harst S, Klink A. Phase field modeling of the microstructure evolution in a steel workpiece under high temperature gradients. Procedia CIRP. 2018. 71: 99-104.

31. Luo k, Li R, Liu JY. Research on composite machining technology of micro-hole EDM-drilling without metamorphic layer. Aerospace Manufacturing Technology. 2023. 66.

32. Zhang Tingliang. Simulation and experimental study on the forming process of remelted layer on EDM surface Harbin Institute of Technology. 2023.